A Noncubic Triply Periodic Network Morphology in Poly(isoprene-*b*-styrene-*b*-ethylene oxide) Triblock Copolymers

Travis S. Bailey, Cordell M. Hardy, Thomas H. Epps, III, and Frank S. Bates*

Department of Chemical Engineering and Materials Science, University of Minnesota, Minneapolis, Minnesota 55455

Received October 1, 2001

ABSTRACT: We present characterization data for linear poly(isoprene-*b*-styrene-*b*-ethylene oxide) (PI−PS−PEO) triblock copolymers containing equal volume fractions of PI and PS ($f_{PI} = f_{PS}$) and varying amounts of PEO, $0 \leq f_{PEO} \leq {}^1/_3$. Detailed characterization by TEM, SAXS, dynamic mechanical spectroscopy, static birefringence, and DSC indicates three distinct morphologies: two-domain lamellae, a three-domain noncubic triply periodic network structure, and three-domain lamellae with increasing PEO content. This phase behavior is in striking contrast with the homologous PS−PI−PEO triblock phase diagram, reported earlier, which contains four different morphologies between the limiting two- and three-domain lamellae phases. Preliminary analysis suggests the noncubic network structure contains elementary units of 3-fold coordination, yet fundamentally distinct from the cubic core−shell gyroid topology previously demonstrated in PS−PI−PEO. This tentatively assigned model is a structural hybrid of the gyroid and perforated lamellar morphologies. These results provide quantitative evidence regarding the effects of block sequencing on the phase behavior of ABC triblock copolymers near the order−disorder transition.

Introduction

Research conducted over nearly three decades, culminating in the mid-1990s, resulted in essentially complete theoretical and experimental descriptions of AB diblock copolymer melt phase behavior.[1] Just four morphologies exist under equilibrium conditions—spheres, cylinders, gyroid, and lamellae—governed by three tunable molecular parameters: the overall degree of polymerization N, the A block volume fraction f_A, and the segment−segment interaction parameter χ_{AB}. More recently, experiments have shown that one additional block can produce remarkable morphological complexity.[2−11] Roughly 20 morphologies have been documented in linear ABC triblock copolymers including core−shell versions of the diblock structures (spheres, cylinders, gyroid, and lamellae), mixed geometry microstructures such as spheres in cylinders, cylinders in lamellae, rings on rods, and the exquisite knitting pattern. Systematizing such phase behavior, analogous to what has been accomplished with diblocks, is challenging, owing to a drastically expanded parameter space. Addition of a third block triples the number of χ parameters (χ_{AB}, χ_{AC}, χ_{BC}), doubles the number of independent composition variables (f_A, f_B, $f_C = 1 - f_A - f_B$), and triples the number of possible block sequences (ABC, ACB, BAC), which translates into an 18-fold increase in the number of possible combinations of these molecular parameters.

Such phase complexity presents considerable challenges to theoreticians as well as experimentalists. Classical self-consistent mean-field theory, which has been so successfully applied to diblock copolymers,[12] begins with a collection of specified phase symmetries. Comparison of the associated computed free energies leads to a prediction for the equilibrium state. This approach also works well with multiblock copolymers[11,13] provided the ordered state symmetries are known in advance. Given the expanded array of known ABC morphologies, and the possibility of many more unknown ones, this technique is less useful as a predictive tool when three or more block types are considered. However, recently Bohbot-Raviv and Wang[14] and Fredrickson et al.[15,16] introduced revolutionary new techniques for computing the equilibrium properties of many component block copolymer systems that do not rely on assumptions regarding phase symmetry. While promising, these predictive computational tools must be validated against equilibrium experimental results as a function of the controllable variables, i.e., f_i, χ_{ij}, N, and the block sequence.

In practice, attacking an expanded parameter space and coordination of the growing number of documented morphologies is further complicated by the experimental uncertainties in f_i and N (including compositional and overall molecular weight polydispersity) inherent in the synthetic and characterization methods employed in producing triblock copolymers. In the first of this series of publications,[17] we introduced a methodology that greatly moderates the impact of these complicating factors. A series of poly(styrene-*b*-isoprene-*b*-ethylene oxide) (PS−PI−PEO) triblock copolymers were prepared from a single batch of monohydroxyl-terminated diblock (PS−PI−OH) by reinitiation with potassium naphthalenide followed by quantitative addition of ethylene oxide. This process eliminates relative variations in composition, thereby permitting the systematic interrogation of phase behavior as a function of one composition variable. Such precision is important for comparison with theory given the dense array of ordered structures encountered over a restricted set of compositions; e.g., six phases were documented over $0 \leq f_{PEO} \leq {}^1/_3$ in the PS−PI−PEO series as illustrated in Figure 1.

In this publication we report the phase behavior for a complementary series of PI−PS−PEO triblock copolymers near the order−disorder transition. The sole

* To whom correspondence should be addressed.

10.1021/ma011716x CCC: $22.00
Published on Web 07/25/2002

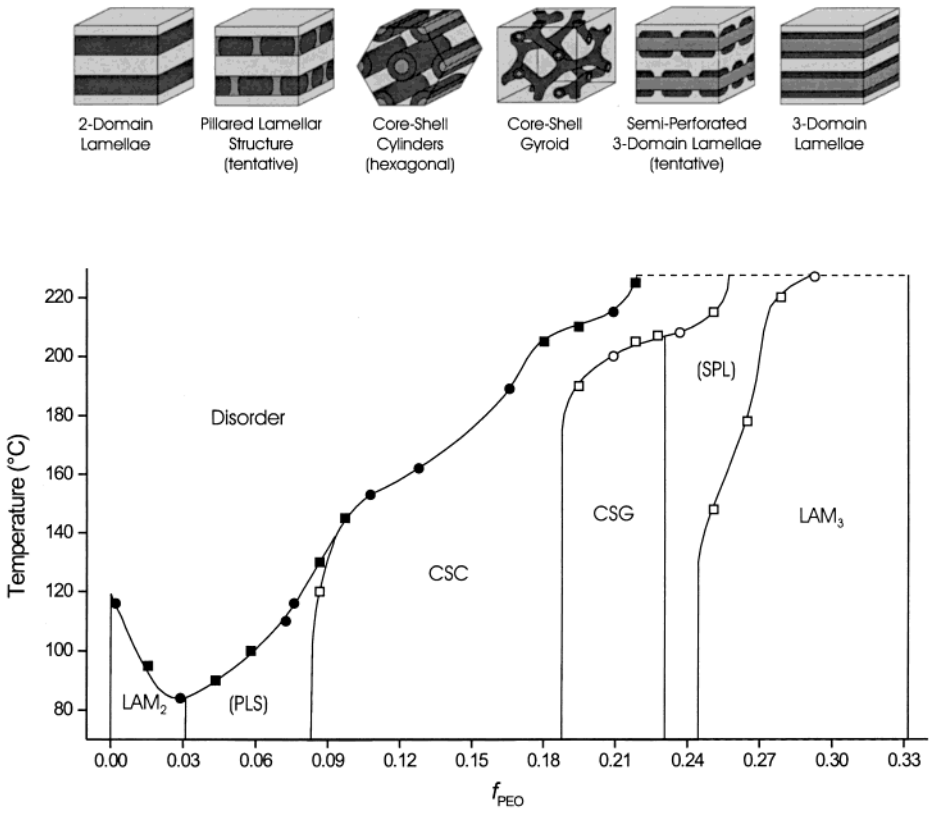

Figure 1. Phase diagram for PS−PI−PEO triblock copolymers along the isopleth $f_{PS} = f_{PI}$ (from Bailey et al.[17]). Four ordered phases separate two-domain (LAM_2) and three-domain (LAM_3) lamellae.

variation in molecular parameters relative to the previous study is the block sequence, in this case PI−PS−PEO vs PS−PI−PEO. Small-angle X-ray scattering (SAXS), dynamic mechanical spectroscopy (DMS), transmission electron microscopy (TEM), static birefringence, and differential scanning calorimetry (DSC) measurements reveal a grossly different phase behavior as a function of PEO composition. Just three ordered phases have been identified over $0 \leq f_{PEO} \leq {}^1/_3$: two-domain lamellae ($LAM_2$) and three-domain lamellae (LAM_3) at the limiting compositions and a new three-domain noncubic ordered phase in between, spanning $0.12 \lesssim f_{PEO} \lesssim 0.24$ and tentatively identified as a triply periodic network structure. These results provide detailed evidence of the profound effects of block sequencing on the equilibrium morphology of ABC triblock copolymers.

Experimental Section

Materials Synthesis. Poly(isoprene-*b*-styrene-*b*-ethylene oxide) (PI−PS−PEO) triblock copolymers were prepared by anionic polymerization exploiting a multistep process in which a series of ethylene oxide polymerizations were initiated from a single batch of hydroxyl-terminated poly(isoprene-*b*-styrene) diblock copolymer. The poly(isoprene) blocks are comprised of 95% 1,4 repeat units. A complete description of the synthetic procedures used in this work has been reported elsewhere.[17]

Chemical Characterization. Molecular weight distributions and polydispersities were obtained by gel permeation chromatography (GPC). GPC measurements were performed using three 5 μm Phenomenex Phenogel columns (10 000, 5000, and 500 Å pore size) in series, in combination with a Waters 717 plus autosampler, a Waters 590 programmable HPLC pump, and a Waters 410 differential refractometer. THF was used as the mobile phase at 25 °C, and polydispersity calculations (Table 1) were based on calibration with polystyrene standards (Polymer Laboratories). The absence of detectable amounts of residual parent diblock copolymer in the GPC traces of the triblock copolymers underscores the efficiency of the hydroxyl end-capping reactions and subsequent reinitiation steps, in agreement with previous reports.[18−20]

Fractional composition was determined using ^{1}H NMR on a Varian 300 MHz instrument, with all samples dissolved in deuterated chloroform. Delay times between acquisitions were set to 30 s to allow for required sample relaxation. Direct quantitative integration was not possible due to overlap of the residual protio solvent and aromatic (styrene) resonances. Accurate quantitative information was obtained by acquiring spectra of both the polymer sample and the pure $CDCl_3$ solvent with TMS and then using the ratio of the $CHCl_3$ to TMS peaks in the blank sample to correct the integration of the sample spectra. Block mole fractions were determined using relative integrated peak intensities and converted to volume fractions using published homopolymer densities reported at 140 °C ($\rho_{PS} = 0.969$ g/cm^3, $\rho_{PI} = 0.830$ g/cm^3, $\rho_{PEO} = 1.064$ g/cm^3).[21] We note that these nominal densities (and thus copolymer volume fractions) are not corrected for relative changes that occur as a function of temperature.

Molecular weights of both triblock copolymers were inferred from ^{1}H NMR spectra and the molecular weight of the precursor diblock copolymer, previously determined by MALDI−TOF mass spectroscopy. Mass spectroscopy was performed using a Bruker Daltonics Reflex III mass spectrometer. Samples were run in a linear mode at 20 kV using a dithranol matrix with Ag^+ cation. The value of M_n obtained by the MALDI technique was within 5% of the value expected from the reaction stoichiometry. Chemical characterization results for all copolymers are listed in Table 1.

Dynamic Mechanical Spectroscopy. All rheological measurements were performed using a Rheometrics Scientific ARES dynamic mechanical spectrometer (DMS) in the 25 mm diameter, parallel plate configuration. Measurements of elastic and loss moduli were obtained as a function of temperature at a constant frequency ($\omega = 1$ rad/s) and a ramp rate (heating and cooling) of 1 °C/min or as a function of frequency at constant temperature, in all cases under a blanket of nitrogen gas. The strain amplitude was carefully chosen for each sample

Table 1. Characterization Results for PI−PS−PEO Triblock Copolymers[a]

sample	M_n (g/mol) (±100 g/mol)	M_w/M_n	f_{PI} (±0.002)	f_{PS} (±0.002)	f_{PEO} (±0.002)	T_{ODT} (°C)
parent diblock						
IS-OH3	13 550	1.05	0.501	0.496	0.003	97
triblock copolymer						
ISO1	13 810	1.05	0.488	0.494	0.019	111
ISO5	14 330	1.05	0.473	0.478	0.049	134
ISO2	14 610	1.06	0.465	0.470	0.065	146
ISO3	15 240	1.05	0.448	0.454	0.098	164
ISO4	15 780	1.05	0.440	0.435	0.125	194
ISO7	16 320	1.05	0.422	0.427	0.150	217
ISO13	16 930	1.06	0.409	0.414	0.177	246
ISO6	17 080	1.05	0.411	0.406	0.183	(251)
ISO8	17 780	1.06	0.392	0.397	0.211	(267)
ISO9	18 520	1.05	0.378	0.383	0.239	(292)
ISO10	19 440	1.06	0.362	0.367	0.271	
ISO11	20 380	1.05	0.347	0.352	0.301	
ISO12	21 770	1.06	0.327	0.331	0.341	

[a] f_i represents the volume fraction of block i based on reported homopolymer densities at 140 °C.

such that measurements were maintained in the linear viscoelastic region of the material, with typical values between 0.3% and 0.8%. Temperature ramp data acquisition was preceded by preliminary heating of the samples to temperatures 5 °C beyond the point of disorder in the sample, defined by a sudden decrease in the elastic modulus to below 1.0 Pa. Data were then collected for the sample while cooling through the order−disorder transition (ODT) back to 70 °C, followed by heating once again through the point of disorder. All ODTs discussed in the text were determined from the final heating traces to avoid including any nonequilibrium effects induced during sample preparation. Isothermal frequency scans were recorded after thermal soak times of at least 10 min.

Samples were prepared as 1.25 mm thick films 25.0 mm in diameter, formed from powders placed in a mold and subsequently hot pressed at 500 psi for 5−7 min. Samples were pressed at temperatures corresponding to the melt state region of the material, near the ODT when possible but never above 200 °C. Confirmation of ODTs suggested by the rheological measurements was made through comparison with SAXS data. Separate DMS and differential scanning calorimetry (DSC) measurements indicated that the PS glass transition and PEO melting temperatures occurred at approximately 75 and 65 °C, respectively.

Small-Angle X-ray Scattering (SAXS). SAXS measurements were made at the Institute of Technology (IT) characterization facility at the University of Minnesota. Copper Kα radiation (wavelength = 1.54 Å) was generated by a Rigaku Ru-200BVH rotating anode using a 0.2 × 2.0 mm^2 microfocus cathode and monochromatized by total reflecting Franks mirrors and a nickel foil filter. Two-dimensional scattering data were collected by a Siemens HI-STAR multiwire area detector. All data were corrected for detector response characteristics prior to analysis. Samples were run under a vacuum atmosphere of several Torr. The scattering data were azimuthally averaged and are reported as a function of the magnitude of the scattering vector $q = (4\pi/\lambda)\sin(\theta/2)$, where θ is the angle between the incident and scattered radiation. Prior to data collection, samples of pure triblock were obtained from pressed films (see preparation of rheology samples above), and SAXS data were collected in a manner analogous to the DMS data. Samples were first annealed (10 min) above the point of disorder when possible (but never above 225 °C) to erase nonequilibrium effects produced during sample preparation. Data were then collected while cooling the sample stepwise to 70 °C and then while heating the sample, again stepwise back through the point of disorder (or to 225 °C). All SAXS data were collected isothermally over a 6 min acquisition period. Ten minute thermal soak times were allowed at each new temperature prior to data acquisition.

Transmission Electron Microscopy (TEM). TEM images also were obtained at the IT characterization facility at the University of Minnesota, using a JEOL 1210 TEM operating at 120 kV. Thin film samples were prepared using a Reichart ultramicrotome fitted with a Microstar diamond knife. Samples generally were cut between −65 and −40 °C and placed on 400 mesh copper grids (Ted Pella). Contrast within the sample was achieved through selective staining of the PI domains using vapor from a 4% aqueous solution of osmium tetroxide (Ted Pella). Samples were exposed to the vapor for between 2 and 5 min.

Polymer samples were prepared for microtoming using the sample chamber of the SAXS instrument, allowing collection of scattering data at all stages of the preparation process. All films were preannealed above their point of disorder (or at the 225 °C limit) prior to decreasing the temperature into the ordered melt state region. Samples were annealed in the melt state until order was established (SAXS) before decreasing the temperature to 80 °C. Samples were held at 80 °C for 10−15 min to allow vitrification of the glassy PS domains, prior to cooling rapidly (30 °C/min) to room temperature (25 °C). Following this strategy the melt morphologies could be maintained adequately, avoiding gross disruption of the morphological structure by crystallization of the PEO domains occurring below 65 °C. Confirmation of a "trapped" morphology was made by comparison of SAXS data of the newly formed samples (at room temperature) with that observed in the melt state. Microtoming, staining, and microscopy of these samples were subsequently carried out with minimal delay (to limit the disruptive effects of PEO crystallization), usually within 36 h of arriving at 25 °C.

Static Birefringence. Static birefringence measurements[22−24] were performed on samples sealed between two glass disks separated by a 1 mm aluminum spacer. Samples were heated above the ODT using an electrically heated copper block thermostated to ±0.2 °C. Sample cooling was unassisted, with rates of at most 1 °C/min maintained through positive input of heat. Light from a 5 mW HeNe laser was passed through the sample, placed between two perpendicularly crossed polarizers. Transmitted depolarized intensity was detected by a photodiode connected to a voltmeter. Nonzero transmitted intensity is attributed to depolarization due to intrinsic and form birefringence characteristic of anisotropic block copolymer domain structure. The absence of birefringence (zero transmitted intensity) is indicative of phase isotropy, associated with disordered and cubic phases. Representative results from this instrument obtained during transitions between isotropic (cubic and disordered) and noncubic (lamellae and cylinders) phases can be found in the literature.[25]

Differential Scanning Calorimetry (DSC). Calorimetry experiments were conducted with a Perkin-Elmer Pyris 1 DSC fitted with a Cryofill liquid nitrogen attachment. Data were acquired during temperature ramps driven at constant heating rate between 10 and 20 °C/min. The focus of these experiments was to extract the heat of melting of the PEO blocks. PEO melting produced well-defined endotherms and the degree of crystallinity was determined by integration after subtraction of the (nearly linear) background heat capacity. The percent

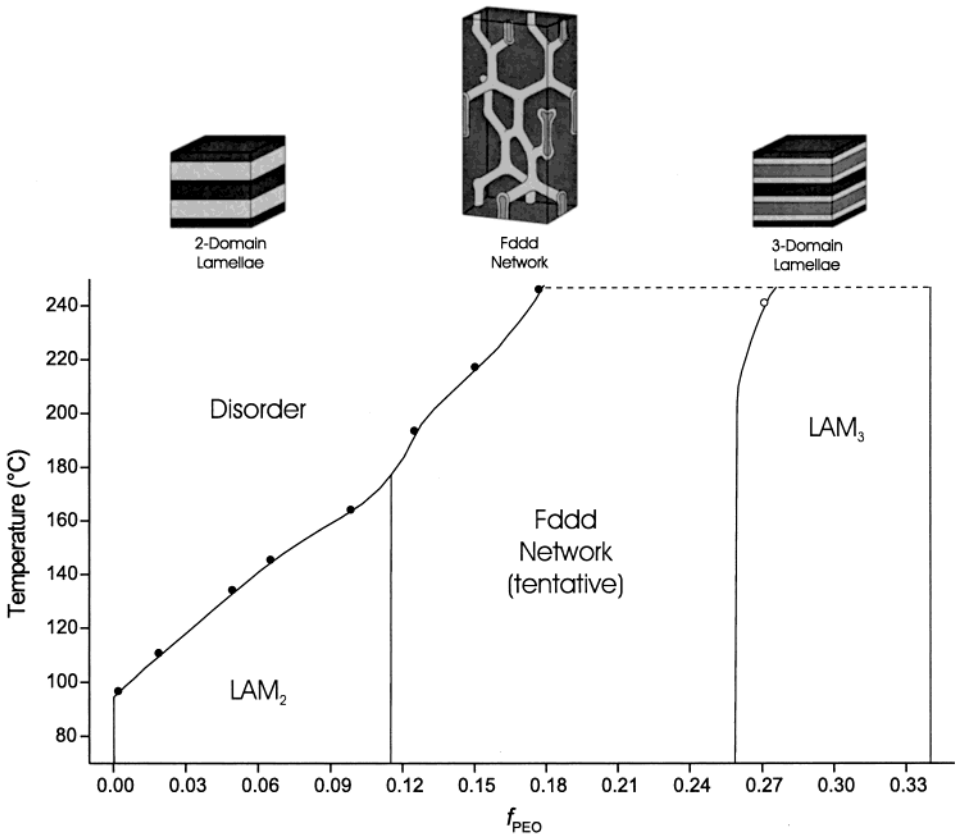

Figure 2. Phase diagram for PI−PS−PEO triblock copolymers along the $f_{PS} = f_{PI}$ isopleth deduced from characterization results reported in this article. One noncubic triply periodic phase lies between the two-domain and three-domain lamellae, tentatively identified as a single network structure with *Fddd* space group symmetry as illustrated in the sketch.

crystallinity within the PEO material was estimated on the basis of the area under the melting peaks, corrected by the weight fraction of PEO in the sample, and normalized to the heat of fusion of bulk PEO (213 J/g).[26]

DSC samples were stored in sealed containers at 0 °C for at least 2 weeks prior to use. Immediately before use, samples were allowed to equilibrate at room temperature before a measured amount (between 3.5 and 6.5 mg) was placed in an aluminum pan and sealed. The system was cooled to −60 °C and allowed to equilibrate prior to performing temperature scans. A heating scan was run up to 200 °C and followed by a cooling scan to −60 °C. At least two heating and cooling cycles were done with each sample.

Results and Analysis

To facilitate this presentation, we provide at the outset the overall phase diagram for the PI−PS−PEO triblock copolymers in Figure 2. This illustration summarizes conclusions drawn from a variety of characterization experiments described in this section. Overall, just one new phase exists between the symmetric two-domain and three-domain lamellae (LAM_2 and LAM_3) limits, denoted the "middle phase".

As greater lengths of PEO are added to the symmetric PI−PS diblock copolymer, T_{ODT} rises nearly linearly. (T_{ODT} values were identified using the well-established dynamic mechanical spectroscopy (DMS) method,[27] omitted here for brevity.) We comment on the differences between this ODT curve and the one found in Figure 1 in the Discussion section. In the remainder of this section experimental data obtained from specimens representative of the three ordered phases are presented and evaluated.

Lamellae Phases. Figure 2 contains two regions associated with a lamellae morphology: LAM_2 and LAM_3 at low and high PEO contents. Figure 3 provides representative SAXS and TEM results that support assignment of a two-domain (PI and mixed PS/PEO) lamellae structure for $0 \leq f_{PEO} \lesssim 0.12$. The TEM image contains only black (OsO_4 stained PI) and white (PS/PEO) stripes, a pattern found in all the TEM images obtained from specimens in this composition window. SAXS patterns displayed a steady decrease in the peak location q^* (i.e., increase in domain spacing d^*, see below) with increasing PEO content, consistent with an increase in the overall molecular weight. Somewhat surprisingly, second-order diffraction is absent in all these powder patterns. This is expected for the symmetric diblock (note the position of the third-order reflection lies outside the q range) but not necessarily for the two-domain triblock; a graded PS/PEO composition profile may contribute to the extinction of the second-order peak. Notwithstanding this lack of higher order scattering, the lamellar morphology is unambiguously established by the TEM data.

Three-domain (PI, PS, and PEO) lamellae, denoted LAM_3, are found at higher PEO compositions, $0.25 \lesssim f_{PEO} \leq 0.33$. Figure 4 provides a SAXS pattern and a representative TEM image taken from the $f_{PEO} = 0.30$ specimen. All three specimens in this region of phase space display second-order reflections at $2q^*$, and striped TEM images like those shown in Figure 4, consistent with a layered structure. Delineating individual PS and PEO domains in this image is nearly impossible since neither block picks up much of the OsO_4 stain. However, close examination of high-magnification versions of the TEM pictures obtained from specimens with varying degrees of staining revealed slightly gray stripes of PEO in the center of the

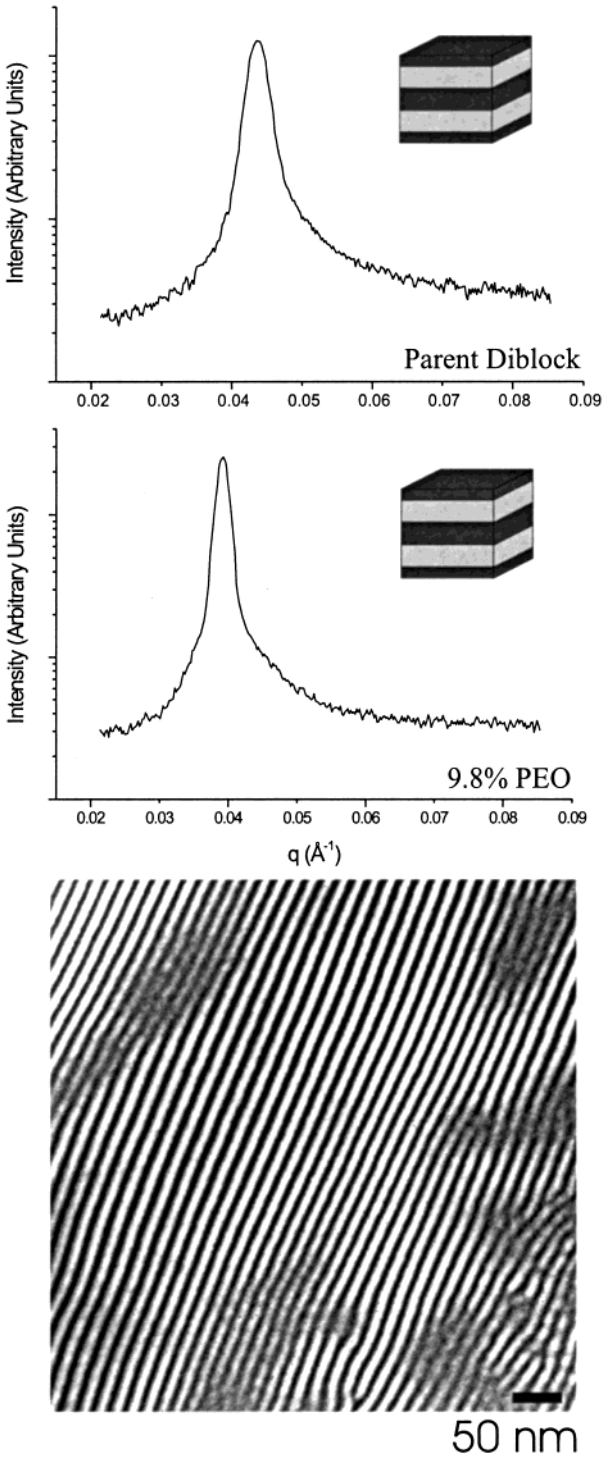

Figure 3. SAXS data from the parent PI−PS diblock copolymer (90 °C, top), and SAXS (155 °C, middle) and TEM (OsO_4 stained, bottom) results from a PI−PS−PEO triblock copolymer containing 9.8 vol % PEO. These results are consistent with two-domain (PI and mixed PS/PEO) lamellae (LAM_2) morphologies.

white regions. (With PS−PI−PEO this was not a problem since the PEO and PS domains were separated by PI.[17]) A peculiar aspect of the micrograph shown here is a regular undulating pattern along the interfaces, clearly absent in Figure 3. We believe this is a consequence of PEO crystallization, which produces local distortions to the microstructure without disrupting the overall domain symmetry. DSC analysis confirmed 50−60% crystallinity within the LAM_3 PEO domains following several weeks at room temperature (see below).

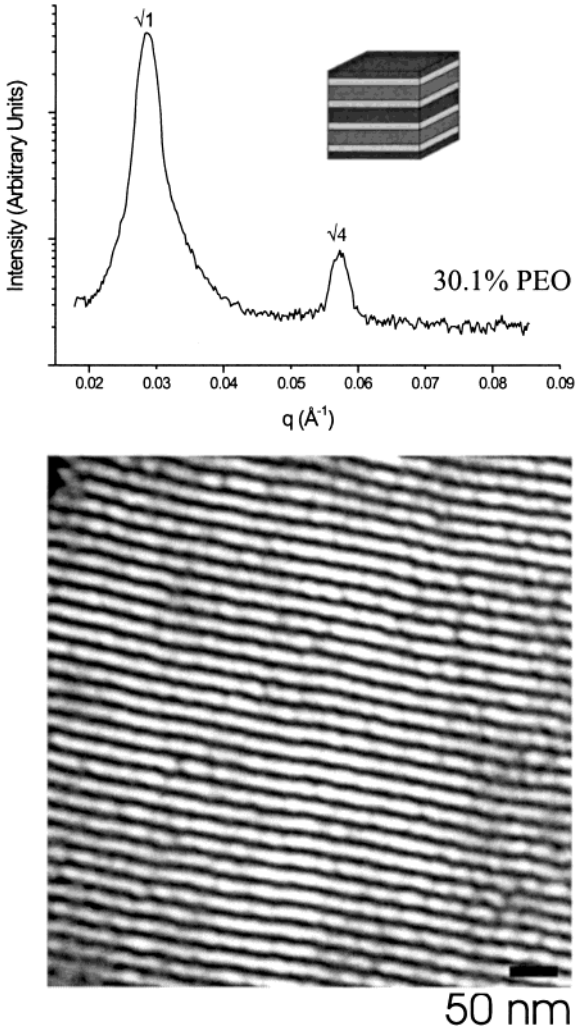

Figure 4. SAXS (180 °C, top) and TEM (OsO_4 stained, bottom) data from the PI−PS−PEO triblock copolymer containing 30% PEO. These results are consistent with a three-domain lamellae (LAM_3) morphology.

Quantitative comparison of the TEM and SAXS patterns in Figures 3 and 4 reveals that within experimental error $d^*_{TEM} \approx d^*_{SAXS}$ for $f_{PEO} = 0.098$, while $d^*_{TEM} \approx (0.80-0.85)d^*_{SAXS}$ for $f_{PEO} = 0.30$, where d^* is the lamellae period. These trends were evident in all the LAM_2 and LAM_3 specimens. We are not certain as to the reasons for the modest inconsistency between the TEM and SAXS results for the three-domain materials although PEO crystallization and possibly degradation in the electron beam would contribute to this effect.

Middle Phase. The most interesting structure encountered in this work occurs over a relatively wide range of compositions, $0.12 \lesssim f_{PEO} \lesssim 0.25$. All the structural features and properties associated with this phase are dramatically different than those characterizing the bordering lamellae. Representative SAXS patterns taken at 130 °C for each of the six specimens displaying the middle phase are presented in Figure 5. Several higher order reflections are evident in these data; however, they do not conform to any familiar morphology. Heating the middle phase produced disorder as documented for the $f_{PEO} = 0.125$ specimen in Figure 6. Between 190 and 200 °C the diffraction pattern loses all higher order reflections, and the principal peak at q^* broadens. This transition is well

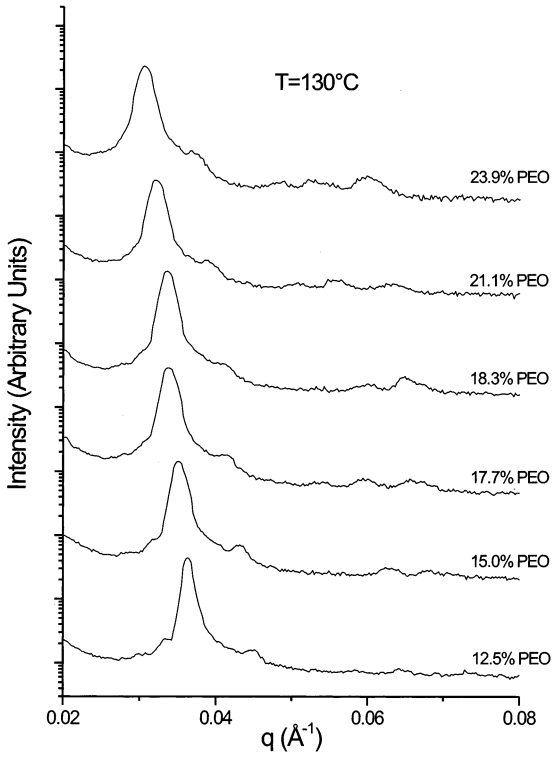

Figure 5. SAXS patterns obtained at 130 °C from PI−PS−PEO triblock copolymers associated with the middle phase (see Figure 2). Increasing the PEO content increases the ordered lattice dimensions without affecting significantly the relative features in these powder patterns.

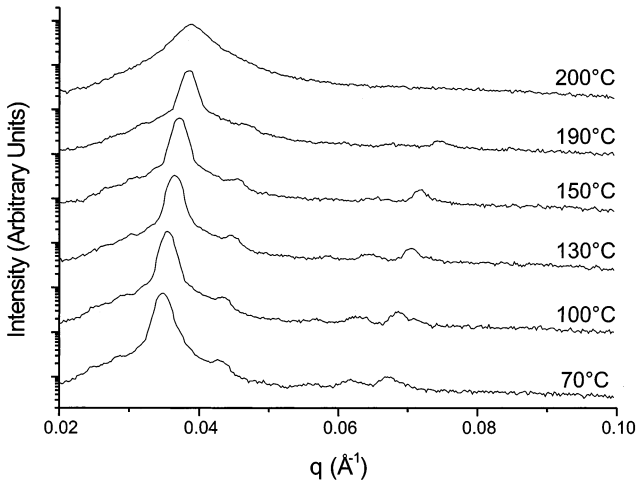

Figure 6. SAXS patterns from the PI−PS−PEO triblock copolymer containing 12.5% PEO recorded as a function of temperature. Loss of higher order reflections and broadening of the principal peak at 200 °C are consistent with a state of disorder.

correlated with a precipitous drop in G' consistent with an order−disorder transition (see below).

The highly elastic nature of this phase is illustrated by frequency sweeps of G' and G'' obtained from the $f_{PEO} = 0.183$ specimen and presented in Figure 7. A nearly frequency-independent dynamic elastic modulus, $G' \cong 6 \times 10^4$ Pa with $G'' \ll G'$, characterizes the middle phase at all but the lowest frequencies and highest temperatures. This type of viscoelastic pattern has been associated with the spherical and gyroid cubic phases in earlier studies.[28] We comment further on the significance of this result in the Discussion section.

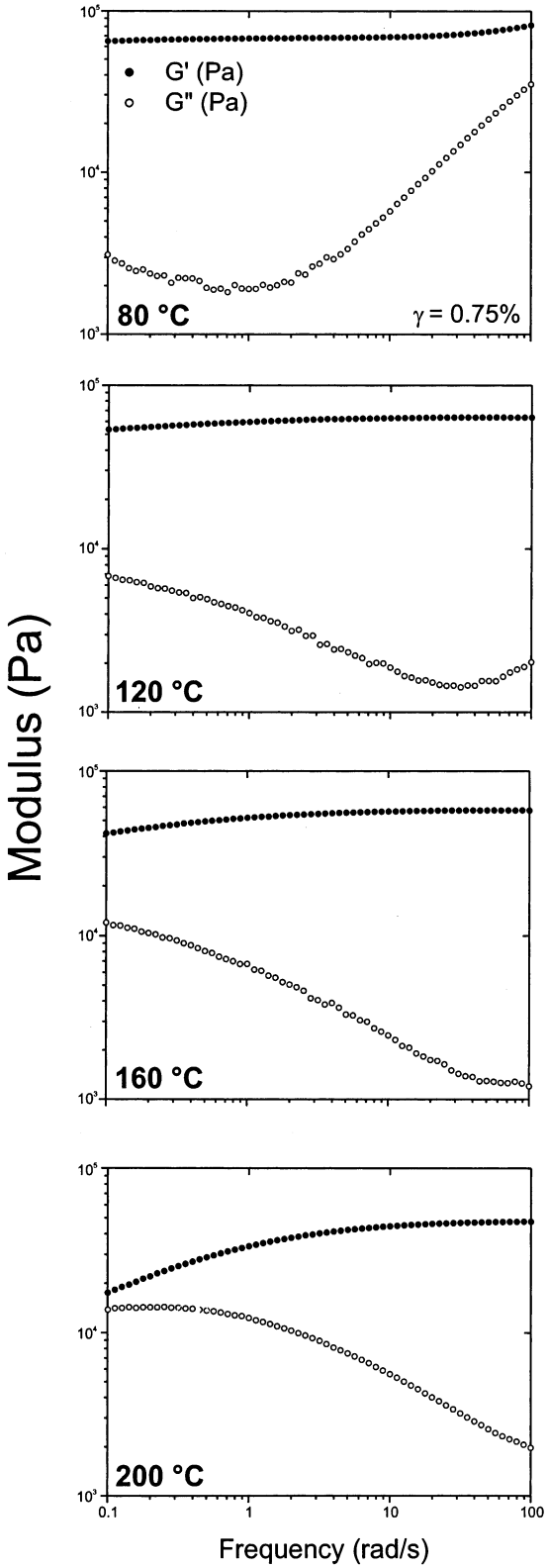

Figure 7. Dynamic mechanical spectroscopy results for the $f_{PEO} = 0.18$ PI−PS−PEO triblock copolymer. This highly elastic behavior, common to all six specimens located in the middle phase window (see Figure 2), is consistent with a triply periodic morphology.[28]

TEM analysis produced two predominate images of the middle phase as shown in Figure 8; these pictures were obtained from the $f_{PEO} = 0.183$ specimen. Both projections evidence long-range translational and rotational order and a morphology different from the LAM_2

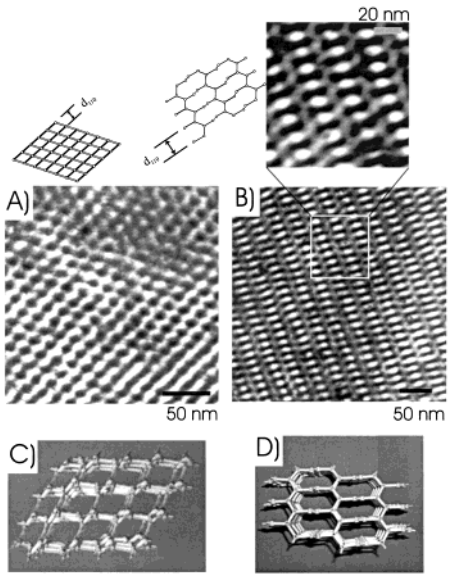

Figure 8. Representative TEM images obtained from the $f_{PEO} = 0.183$ PI−PS−PEO specimen. Black and white regions correspond to OsO_4 stained PI and unstained PS and PEO regions, respectively. These complex structures are associated with two-dimensional projections of a single network structure comprised of 3-fold connectors with *Fddd* space group symmetry (see Figure 11). Two orientations of this lattice, consistent with the TEM images, are shown below each micrograph. Open channels correspond to PI (block), while the white regions are associated with PS and PEO, which are not stained. Gray zigzag channels, most evident in the expanded panel (from a different micrograph of the same area), are interpreted as PS and PEO, embedded in PI.

and LAM_3 phases or any other common morphology. One image, containing an expanded view, exhibits three distinct levels of contrast, white, gray, and black. We return to these micrographs in the Discussion section.

DSC determined percent of crystallinity in the PEO components of these triblock copolymers is plotted as a function of composition in Figure 9, along with the principal period $d^* = 2\pi/q^*$ obtained from the first-order SAXS reflections. The transition from LAM_3 to the middle phase with decreasing PEO content does not affect the degree of crystallinity, suggesting that both structures contain relatively unencumbered pure PEO domains. From this we tentatively deduce that the middle phase is a three-domain structure. In contrast, the transition to LAM_2 is accompanied by a significant and discontinuous loss in PEO crystallinity consistent with a mixed PS−PEO domain structure. Within the precision of the SAXS measurements, d^* exhibits no discernible correlation with phase changes as a function of f_{PEO}.

Our final characterization technique for the middle phase is static birefringence (SB). Figure 10 contains the results from SB measurements conducted while cooling the $f_{PEO} = 0.125$ specimen from above the ODT at 1 °C/min, along with isochronal DMS data (G' and G'') obtained under the same conditions. Above approximately 195 °C the triblock melt is devoid of birefringence, consistent with an isotropic state, i.e., disorder. Below this temperature a significant SB signal develops coincident with an increase of more than 3 orders of magnitude in G'. The magnitude of this birefringence signal at T_{ODT} equals or exceeds that registered for disorder-to-cylinder and disorder-to-lamellae transitions in PS−PI solutions.[25] On the basis

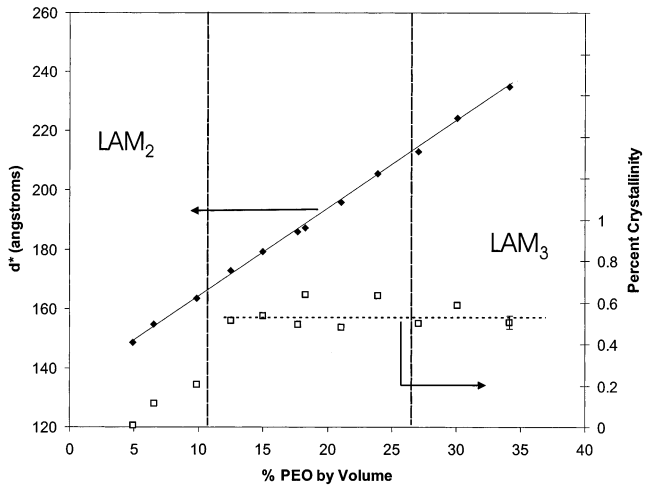

Figure 9. Principal spacing $d^* = 2\pi/q^*$ from SAXS data at 130 °C and percent PEO crystallinity obtained from DSC analysis as a function of PEO composition in the PI−PS−PEO triblock copolymers. Increasing the PEO content expands the ordered state lattice without evidence of morphology changes. Crystallization of the PEO blocks at low temperature is unaffected by the transition from the LAM_3 to middle phase morphology but drops precipitously at the LAM_2 transition. This result is consistent with a three-domain assignment for the middle phase and a two-domain assignment (PI and mixed PS and PEO) for the low composition lamellar phase.

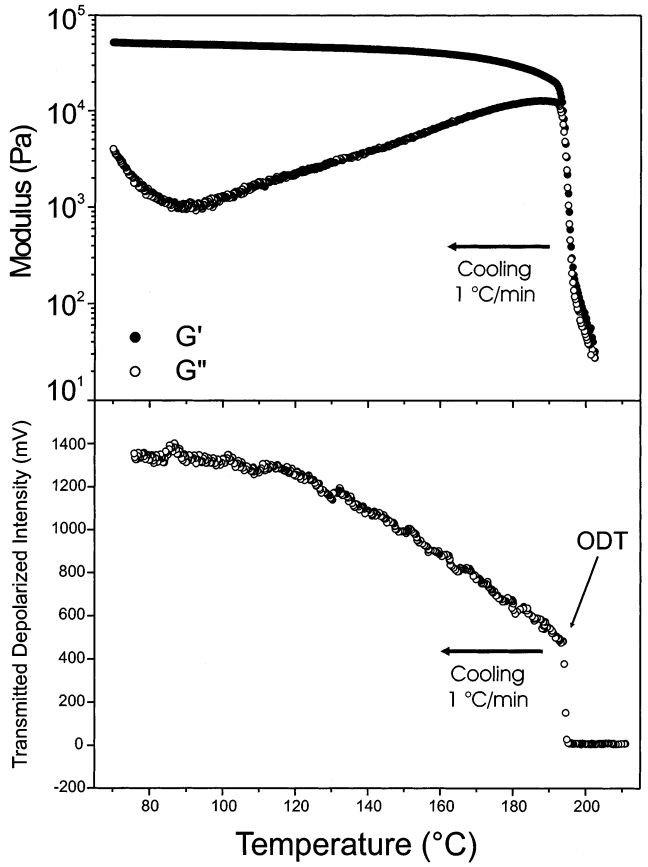

Figure 10. Development of dynamic mechanical moduli (top) and static birefringence (bottom) as the $f_{PEO} = 0.125$ specimen was cooled at 1 °C/min from the disordered to the ordered states. The lack of birefringence above T_{ODT} is consistent with an isotropic disordered morphology while the strong signal in the ordered phase is indicative of a noncubic lattice.

of the previously described SAXS and DMS experiments, this jump in birefringence reflects a disorder-to-order

transition. With cooling the SB intensity increases, more than doubling between 195 and 80 °C, consistent with the development of stronger segregation. These results indicate that the middle phase is not optically isotropic from which we deduce that the ordered state symmetry is noncubic.[22−24]

Discussion

Rearranging the block sequence from PS−PI−PEO to PI−PS−PEO produces gross changes in phase behavior near the order−disorder transition. Comparison of Figures 1 and 2 reveals qualitative differences in the composition dependence of T_{ODT} and a reduction in the number of ordered phases from four to one, respectively, between the common limiting LAM_2 and LAM_3 morphologies. These issues are considered in this section.

Order−Disorder Transition. The temperature dependence of the LAM_2-to-disorder transition is sensitive to block sequencing. Whereas this ODT temperature increases with PEO content in PI−PS−PEO (Figure 2), it decreases in PS−PI−PEO (Figure 1). This behavior can be rationalized on the basis of the associated segment−segment interaction parameters $\chi_{PI-PS} \approx \chi_{PS-PEO} > \chi_{PI-PEO}$. In both systems addition of a small PEO block is not adequate to induce separation of a third domain. With PS−PI−PEO the PEO block is forced to make contact with PI, creating the least favorable segment−segment interactions. In this case suppression of T_{ODT} with increasing PEO length is favored since the disordered state provides some degree of screening of unfavorable PI and PEO contacts by PS segments. Once sufficiently long the PEO blocks segregate into a third domain, thereby minimizing the enthalpic mixing penalty. This occurs at $f_{PEO} \approx 0.03$ (Figure 1) after which T_{ODT} increases with increasing PEO block length.

PI−PS−PEO differs in two ways. First, T_{ODT} increases with increasing PEO content over the entire LAM_2 phase window, and second this morphology extends up to $f_{PEO} \cong 0.12$. Both differences can be explained on the basis of the sequence of χ parameters. In this instance disordering is not favored as it introduces additional unfavorable PI and PEO contacts relative to the LAM_2 state. Moreover, since PS and PEO are more compatible than PI and PEO, a mixed PS/PEO domain persists to higher f_{PEO} than in the PS−PI−PEO case. These trends in T_{ODT} are anticipated by the RPA theory as shown in a separate publication.[29]

Middle Phase. The most distinctive feature of the PI−PS−PEO phase diagram is the single ordered middle phase bracketed by the LAM_2 and LAM_3 states. We have not yet obtained sufficient characterization data to definitively identify this new morphology. However, based on the compliment of results presented in the previous section, a tentative assignment can be suggested.

Several characteristics of the middle phase have been firmly established. Based on the strong static birefringence documented in Figure 10, the middle phase is not isotropic, which excludes the core−shell gyroid and all other cubic symmetries. However, the DMS measurements shown in Figure 7 are highly suggestive of a triply periodic structure. A frequency-independent linear elastic modulus in an unoriented (polydomain) ordered material implies that an energy barrier exists toward mechanical deformation for all unit cell orientations. Nearly identical results have been reported for spheres packed on a cubic lattice and the gyroid network phase, in diblock and triblock forms.[28] In contrast, cylinders packed on a hexagonal lattice and lamellae (formally a smectic liquid crystal) are characterized by power law relationships in the low-frequency limit $\omega \rightarrow 0$, $G' \sim \omega^m$, $G'' \sim \omega^n$, where $m < 1$ and $n < 1$ (e.g., for lamellae $m \approx n \approx {}^1/_2$).[28] Each of these systems can dissipate stress by sliding along an unrestricted crytallographic axis. Triply periodic structures are solids (crystals) and accordingly display a frequency-independent linear elastic modulus. Triply periodic soft materials are no exception. (The turn down in G' and upturn in G'' at the lowest frequencies and highest temperature in Figure 7 can be attributed to defects as discussed in ref 28.) Mechanical distortion stores elastic energy regardless of orientation until yielding occurs at sufficiently high stress. Prior experiments with block copolymer cubic phases (spheres and gyroid)[28] document precisely the dynamic mechanical response found in Figure 7, leading us to deduce that the middle phase also is a true solid; note these arguments apply to cubic and noncubic structures alike. Thus, we have good reason to believe that the middle phase contains a noncubic triply periodic lattice.

We now turn to the microscopy evidence. Visualization of the morphology by TEM primarily resulted in two distinct image types for the middle phase samples, each presented in Figure 8. In both images, the PI endblock has been stained with OsO_4 to provide contrast with the PS and PEO domains, neither of which reacted to a significant extent with the heavy metal oxide. With little or no staining contrast to distinguish these two adjacent domains, the TEM images presented here offer no means of discerning the exact geometry of the PS/PEO interface; fortunately, the unfavorable χ_{PI-PEO} and PS−PEO block connectivity essentially ensures the PEO segments remain fully contained within the PS domains without formation of an additional PI/PEO interface. Moreover, the DSC data found in Figure 9 support a three-domain (i.e., PI, PS, and PEO) morphology. We return to the issue of the PS/PEO interfacial geometry later in the discussion.

The TEM image in Figure 8a superficially reveals what appear to be PI domains hexagonally arranged in an unstained PS/PEO matrix. More careful inspection uncovers subtle complexities, suggesting the honeycomb appearance of the unstained PS/PEO domains is, in fact, a projected image of a far more complex phase. It is clear that such an image can be created from a variety of microstructures containing 6- or 3-fold projected patterns (e.g., cylinders, gyroid ($Ia\bar{3}d$ and $I4_132$), and perforated lamellae).[2,9,11,27,30,31] In fact, Figure 8a closely resembles the [001] TEM projections from a PI-rich gyroid ($Ia\bar{3}d$) network phase, except for the 4-fold symmetry.[31] That the structure of these samples is complex in three dimensions is supported by the TEM image in Figure 8b. Perhaps the most striking feature in this micrograph is the very noticeable array of stain deficient spots, indicative of continuous channels of PS/PEO oriented perpendicular to the sample's surface. Similarly revealing are the undulating channels extending along the length of the sample. These "accordion-like" undulations are consistent with a planar (graphite-like) assembly of 3-fold connected nodes, with the dilution of contrast indicative of inclusion within stained PI domains.

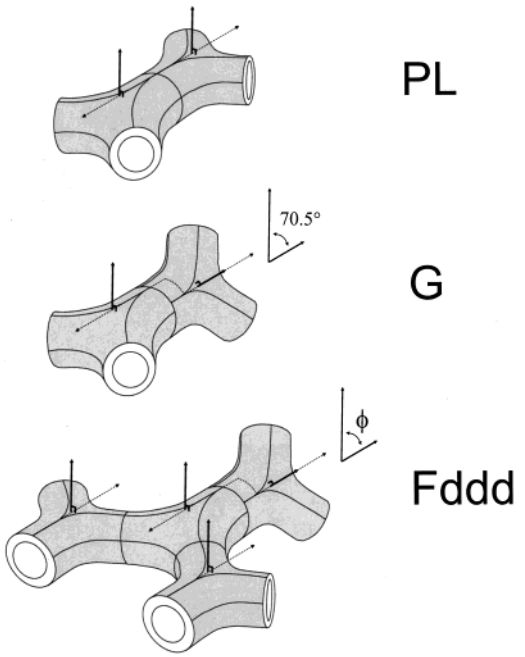

Figure 11. Local configuration of 3-fold connectors in perforated layer (PL), gyroid (G), and the tentatively assigned network morphology with *Fddd* space group symmetry. The complete *Fddd* lattice is constructed from two parts PL and one part G (with some distortion in ϕ).

Because of the considerable frequency with which we could obtained images possessing these distinct features, we have concluded that these two types of channels (in-plane and perpendicular to the plane) are simply different directional orientations of the same structural element. That is, by rotating the sample until the in-plane channels become perpendicular to the surface, the presented image would be reproduced. On the basis of these observations, we concluded these images are consistent with a three-dimensional network of PS/PEO percolating through a continuous PI matrix. (The DSC results shown in Figure 9 indicate a three-domain morphology. However, we cannot ascertain whether the PEO blocks form a continuous core or discontinuous domains surrounded by PS.) Interestingly, we found OsO_4 vapor to permeate bulk samples (10 mm^3) from this region with great efficiency, in contrast to the lamellae samples. Although far from conclusive, this qualitative observation is consistent with the proposed continuity of the PI matrix. Overall, the TEM images suggest a network morphology.

From this collection of experimental data, we have constructed a three-dimensional network model using 3-fold coordinated elementary units ("nodes") connected by a single set of "tubes" (Figure 11). In this model, each node is connected to two others forming one-dimensional, planar zigzag strips. The third connection at every node is used to join adjacent zigzag strips at a specific angle ϕ. Two projections of the resulting orthorhombic network structure (space group Q_{Fddd}, No. 70)[32] with $\phi \sim 60°$ are presented in Figure 8 and two more in Figure 12. In Figure 8 the orientations of this proposed structure have been chosen to coincide with the associated TEM images. Small sketches indicate the 2-dimensional projections and a common (110) plane. Open channels in the model correspond to (stained) PI in the TEM images.

Notably, this three-dimensional network structure is a variation of the well-known "$ThSi_2$-net", which is tetragonal ($\phi = 90°$) in its most symmetric form ($Q_{I41/amd}$, No. 141),[33,34] as shown in Figure 12a. This network topology is particularly unique in that the angle ϕ can be adjusted continually through a concerted rotation about struts adjoining the zigzag strips. Lattices in which ϕ is different from 90° appear to be "sheared", and thus ϕ is often referred to as a shear or distortion angle. A direct comparison of the tetragonal and sheared orthorhombic network lattices is illustrated in Figure 12. When $\phi = 70.5°$, this single network model becomes an exact hybrid of the familiar gyroid (G) and perforated layer (PL) morphologies, with a stoichiometry of one G per two PL 3-fold nodes (see Figure 11).

Several inorganic crystal systems based on this generalized lattice form actually achieve optimum packing of the molecular constituents through adjustment of the shear angle.[35−37] In our block copolymer system, we speculate that, by adopting an angle in the vicinity of 60°, the packing frustration is significantly reduced relative to that present in the tetragonal form. This is perhaps best demonstrated by the recognizing the hexagonal arrangement (as opposed to a tetragonal arrangement) of struts parallel to the [001] direction that results when the structure is sheared to the orthorhombic form of *Fddd* symmetry. This shift is highlighted in Figure 12.

This single network model appears to be consistent with all our characterization data. It is noncubic (hence birefringent) and triply periodic (thus elastic). Figure 8 illustrates two lattice orientations (for $\phi = 60°$) that capture the qualitative TEM features. The [110] direction is particularly interesting. Parallel and perpendicular zigzag chains of PS/PEO would account for the gray and white elements, respectively, while the open channels in the model correlate with columns of stained PI in Figure 8b.

Figure 13 contains a 2-dimensionsal SAXS pattern obtained from the $f_{PEO} = 0.125$ specimen. This diffraction pattern emerged from a sample that had been slowly cooled from the disordered state to 170 °C (T_{ODT} = 194 °C). Fortuitously, a limited number of ordered domains (crystals) were intercepted at the Bragg condition leading to single crystal diffraction, rather than powder diffraction as occurred most generally. (In fact, this result was unusual, and we have not yet established a protocol for reproducibly creating this type of scattering behavior. Nonetheless, this image provides a very useful set of data for analysis.) Also shown in Figure 13 is a 1-dimensional azimuthally averaged version of this diffraction pattern. Comparison with the results in Figures 5 and 6 confirms near exact consistency. Also included in Figure 13 are all the allowed reflections for the *Fddd* space group ($\phi = 60°$)[32] over the working range of the SAXS data, where the (111) reflection has been arbitrarily identified with the first-order peak.

These SAXS results contain valuable, although incomplete, information regarding our model assignment. There are many more allowed reflections than identifiable SAXS peaks. Resolution limitations preclude a proper indexing even with a better signal-to-noise. Nevertheless, the first- and second-order experimental reflections are nicely accommodated by the (111) (or (004)) and (113) allowed diffraction conditions. Careful inspection of the 2-dimension scattering pattern confirms that the four powder pattern peaks found in Figures 5 and 6 in fact derive from actual Bragg scattering. Without a simulated scattering calculation

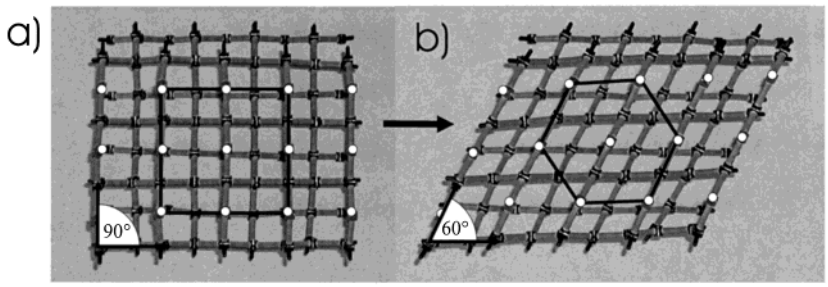

Figure 12. Illustration of shear distortion in the *Fddd* network model. These images correspond to the [001] direction with (a) $\phi = 90°$ and (b) $\phi = 60°$.

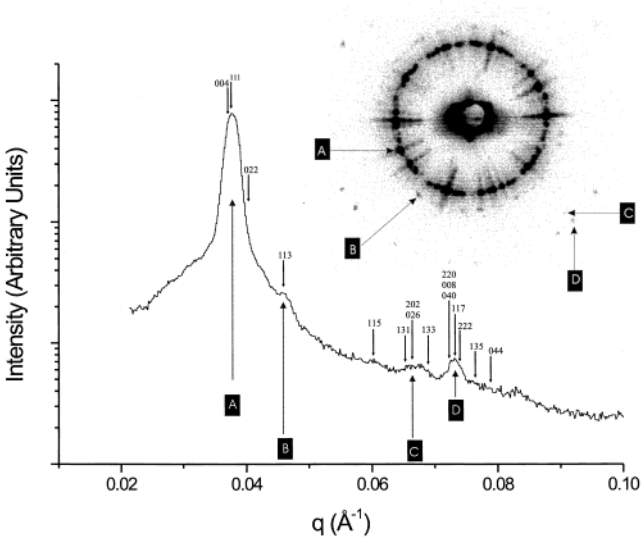

Figure 13. Two-dimensional, and the associated azimuthally averaged, SAXS patterns obtained from the $f_{PEO} = 0.125$ PI−PS−PEO specimen at 170 °C. Four distinct orders of reflection, evident as single-crystal diffraction in the two-dimensional pattern, are identified in the one-dimensional trace (also see Figures 5 and 6). Allowed reflections for the *Fddd* space group are indicated by the arrows where the principal reflection has been associated with the {111} spacing with $\phi = 60°$.

that includes relative domain electron densities, we cannot weight the relative intensities of these hypothetical reflections nor comment on possible form factor extinctions. And there are simply too many first-order diffraction spots to associate with the few higher order peaks to establish the underlying angular relationships. On the basis of the *Fddd* network model, we obtain a 15%−20% smaller lattice spacing from the TEM pictures (Figure 8) than the SAXS data (Figure 5). This inconsistency mirrors that identified earlier with the LAM_3 specimens and presumably derives from the same phenomena, i.e., PEO crystallization, electron beam degradation, and possibly staining artifacts. Although we cannot be certain as to the exact origins of this effect, both the sign and magnitude of this problem have been reported before.[38]

Another striking feature of the 2-dimensional scattering pattern are the radial streaks coincident with the first-order diffraction spots. Close examination reveals two, and perhaps even three, weak intensity undulations on the low-q side of the strong principal Bragg peaks; this leads to the shoulder at low q in the 1-dimensional trace. We are not certain as to the origins of this effect although we suspect it may be associated with finite ordered domain dimensions. For example, thin, uniform, platelike crystals would produce two types of interference: Bragg diffraction at $\mathbf{q}^*$ (and higher order reflections) and periodic undulations in intensity with a frequency $\mathbf{q}_\perp = 2\pi/L$, where L is the crystal thickness and $\mathbf{q}_\perp$ is the wavevector normal to the crystal face. If the principal crystallographic planes (e.g., (111) according to Figure 13) end up parallel to the crystal faces, then a convolution of both forms of interference will be recorded along radial directions in the 2-dimensional SAXS patterns provided the domains (crystals) are properly aligned. (Specular X-ray or neutron reflection from thin films of block copolymer containing planes of lamellae or cylinders parallel to the surfaces is exactly analogous.[39]) This coincidence would reflect preferred growth directions during ordering from the disordered state.[40]

As a final topic of discussion, we return to the idea that manipulation of the shear angle (ϕ) could permit minimization of packing frustration within the model network. We believe this may be a very real possibility given the wide range of compositions over which this morphology forms (between approximately 12 and 25 vol % PEO along the $f_{PI} = f_{PS}$ compositional isopleth, 3 times the extent of the core−shell gyroid phase in Figure 1). The *Fddd* symmetry applies to any angle ϕ (90° is a special case of higher symmetry), with only the relative values of the three lattice constants changing as a function of ϕ ($a = (c/\sqrt{3}) \sin(\phi/2)$; $b = (c/\sqrt{3}) \cos(\phi/2)$; c). Simple analysis of the network structure reveals that for a given value of c the unit cell volume increases with increasing shear angle according to the relationship $V = (c^3/6) \sin \phi$. The overall volume attributed to the network, in contrast, remains *independent* of ϕ, as no deformation of the structure, only rotation about the struts, occurs during a change in ϕ; of course, this assumes a stiff interfacial structure like the tubular model in Figure 11. Thus, the matrix volume is maximized by shifting the angle toward the most "open" structure, $\phi = 90°$. This shear adjustment mechanism might also explain why d^* apparently is unaffected by the LAM_2 to middle phase to LAM_3 transitions.

Conclusions

We have evaluated the role of block sequencing in linear PS−PI−PEO and PI−PS−PEO triblock copolymers along the $f_{PI} = f_{PS}$ compositional isopleth with $0 \le f_{PEO} \le {}^1/_3$ near the order−disorder transition. Switching the sequence from PS−PI−PEO to PI−PS−PEO has a profound effect on the phase behavior between the two- and three-domain lamellae limits. Whereas four ordered structures separate the LAM_2 and LAM_3 states in PS−PI−PEO, only one (new) ordered morphology spans the composition space between these limiting states in PI−PS−PEO. On the basis of SAXS, DMS, TEM, static birefringence, and DSC measurements, we propose a noncubic triply periodic network model for

this phase constructed from 3-fold connectors that form a structural hybrid between the perforated lamellae and gyroid morphologies. This tentative model has *Fddd* space group symmetry and can be distorted (sheared) continuously, which may account for the remarkably wide range of compositions ($0.12 \lesssim f_{PEO} \lesssim 0.25$) over which it has been found.

Acknowledgment. We thank Michael Ward, Travis Holman, and Victor Young for their helpful discussions concerning molecular crystal networks and space group analysis. We also acknowledge valuable theoretical insights provided by Mark Matsen and Francois Drolet. This work was supported by the National Science Foundation through Grant DMR-9905008 and the MRSEC at the University of Minnesota, which maintains much of the characterization equipment employed.

References and Notes

(1) Bates, F. S.; Fredrickson, G. H. *Phys. Today* **1999**, *52*, 32.
(2) Matsushita, Y.; Suzuki, J.; Seki, M. *Physica B* **1998**, *248*, 238.
(3) Brinkmann, S.; Stadler, R.; Thomas, E. L. *Macromolecules* **1998**, *31*, 6566.
(4) Breiner, U.; Krappe, U.; Thomas, E. L.; Stadler, R. *Macromolecules* **1998**, *31*, 135.
(5) Breiner, U.; Krappe, U.; Jakob, T.; Abetz, V.; Stadler, R. *Polym. Bull. (Berlin)* **1998**, *40*, 219.
(6) Breiner, U.; Krappe, U.; Abetz, V.; Stadler, R. *Macromol. Chem. Phys.* **1997**, *198*, 1051.
(7) Krappe, U.; Stadler, R.; Voigt-Martin, I. *Macromolecules* **1995**, *28*, 4558.
(8) Beckmann, J.; Auschra, C.; Stadler, R. *Macromol. Rapid Commun.* **1994**, *15*, 67.
(9) Hückstädt, H.; Goldacker, T.; Göpfert, A.; Abetz, V. *Macromolecules* **2000**, *33*, 3757.
(10) Mogi, Y.; Nomura, M.; Kotsuji, H.; Ohnishi, K.; Matsushita, Y.; Noda, I. *Macromolecules* **1994**, *27*, 6755.
(11) Shefelbine, T. A.; Vigild, M. E.; Matsen, M. W.; Hajduk, D. A.; Hillmyer, M. A.; Cussler, E. L.; Bates, F. S. *J. Am. Chem. Soc.* **1999**, *121*, 8457.
(12) Matsen, M. W.; Bates, F. S. *Macromolecules* **1996**, *29*, 1091.
(13) Matsen, M. W. *J. Chem. Phys.* **1998**, *108*, 785.
(14) Bohbot-Raviv, Y.; Wang, Z.-G. *Phys. Rev. Lett.* **2000**, *85*, 3428.
(15) Drolet, F.; Fredrickson, G. H. *Phys. Rev. Lett.* **1999**, *83*, 4317.
(16) Fredrickson, G. H.; Ganesan, V.; Drolet, F. *Macromolecules* **2002**, *35*, 16.
(17) Bailey, T. S.; Pham, H. D.; Bates, F. S. *Macromolecules* **2001**, *34*, 6994.
(18) Hillmyer, M. A.; Bates, F. S. *Macromolecules* **1996**, *29*, 6994.
(19) Quirk, R. P.; Ma, J. J. *J. Polym. Sci., Part A: Polym. Chem.* **1988**, *26*, 2031.
(20) Morton, M.; Fetters, L. J.; Inomata, J.; Rubio, D. C.; Young, R. N. *Rubber Chem. Technol.* **1976**, *49*, 303.
(21) Fetters, L. J.; Lohse, D. J.; Richter, D.; Witten, T. A.; Zirkel, A. *Macromolecules* **1994**, *27*, 4639.
(22) Balsara, N. P.; Garetz, B. A.; Dai, H. J. *Macromolecules* **1992**, *25*, 6072.
(23) Balsara, N. P.; Perahia, D.; Safinya, C. R.; Tirrell, M.; Lodge, T. P. *Macromolecules* **1992**, *25*, 3896.
(24) Garetz, B. A.; Newstein, M. C.; Dai, H. J.; Jonnalagadda, S. V.; Balsara, N. P. *Macromolecules* **1993**, *26*, 3151.
(25) Hanley, K. J.; Lodge, T. P.; Huang, C.-I. *Macromolecules* **2000**, *33*, 5918. The authors inadvertently omitted the intensity scale in Figure 2 of this publication. Each marked increment represents 100 mV response (personal communication with T. P. Lodge).
(26) Wunderlich, B. *Macromolecular Physics*; Academic Press: New York, 1980; Vol. 3.
(27) Khandpur, A. K.; Foerster, S.; Bates, F. S.; Hamley, I. W.; Ryan, A. J.; Bras, W.; Almdal, K.; Mortensen, K. *Macromolecules* **1995**, *28*, 8796.
(28) Kossuth, M. B.; Morse, D. C.; Bates, F. S. *J. Rheol.* **1998**, *43*, 167.
(29) Cochran, E. W.; Bates, F. S. *Macromolecules*, submitted.
(30) Hajduk, D. A.; Harper, P. E.; Gruner, S. M.; Honeker, C. C.; Kim, G.; Thomas, E. L.; Fetters, L. J. *Macromolecules* **1994**, *27*, 4063.
(31) Avgeropoulos, A.; Dair, B. J.; Hadjichristidis, N.; Thomas, E. L. *Macromolecules* **1997**, *30*, 5634.
(32) *32.International Tables for X-ray Crystallography*, 3rd ed.; Hahn, T., Ed.; Kluwer Academic Publishers: Boston, MA, 1992.
(33) Batten, S. R.; Robson, R. *Angew. Chem., Int. Ed. Engl.* **1998**, *37*, 1460.
(34) Wells, A. F. *Three-Dimensional Nets and Polyhedra*; John Wiley and Sons: New York, 1977.
(35) Zachariasen, W. H. *J. Chem. Phys.* **1936**, *4*, 618.
(36) Prince, E. *Acta Crystallogr.* **1975**, *B31*, 2536.
(37) Follner, H. *Acta Crystallogr.* **1970**, *B26*, 1544.
(38) Berney, C. V.; Cohen, R. E.; Bates, F. S. *Polymer* **1982**, *23*, 1222.
(39) Russell, T. P. *Physica B* **1996**, *221*, 267.
(40) Dai, H. J.; Balsara, N. P.; Garetz, B. A.; Newstein, M. C. *Phys. Rev. Lett.* **1996**, *77*, 3677.

MA011716X